Supplementary Material for: Fragmentation Dynamics of CS_2 Dications and Trications Following S 2p Ionization

Felix Allum,[1,2,3,†] Chow-shing Lam,[4] Benjamin Erk,[3] Hubertus Bromberger,[3] Philip H. Bucksbaum,[2,5,6] Mathew Britton,[1,2] Michael Burt,[4] Nagitha Ekanayake,[3] Ian Gabalski,[2,5] Diksha Garg,[3] Eva Gougoula,[3] David Heathcote,[4] Andrew J. Howard,[2,5] Paul Hockett,[7] David M. P. Holland,[8] Sonu Kumar,[3,9] Jason W. L. Lee,[3] Joseph McManus,[4] Jochen Mikosch,[10] Dennis Milešević,[4] Russell S. Minns,[11] Christina C. Papadopoulou,[3] Christopher Passow,[3] Weronika O. Razmus,[11] Anja Röder,[12] Daniel Rolles,[13] Arnaud Rouzée,[12] Michael Schuurman,[7,14] Alcides Simao,[15] Albert Stolow,[7,14,16,17] Atia-Tul-Noor,[3] James Unwin,[4] Claire Vallance,[4] Tiffany Walmsley,[4] Mark Brouard,[4] and Ruaridh Forbes[1,18,‡]

[1]*Linac Coherent Light Source, SLAC National Accelerator Laboratory, Menlo Park, CA 94025, USA*

[2]*Stanford PULSE Institute, SLAC National Accelerator Laboratory, Menlo Park, CA 94025, USA*

[3]*Deutsches Elektronen-Synchrotron DESY, Notkestr. 85, 22607 Hamburg, Germany*

[4]*Chemistry Research Laboratory, Department of Chemistry, University of Oxford, Oxford, OX1 3TA, UK*

[5]*Department of Applied Physics, Stanford University, Stanford, CA 94305-4090, USA*

[6]*Department of Physics, Stanford University, Stanford, CA 94305-4013, USA*

[7]*National Research Council Canada, 100 Sussex Drive, Ottawa, Ontario, K1A 0R6, Canada*

[8]*Daresbury Laboratory, Daresbury, Warrington, Cheshire WA4 4AD, UK*

[9]*Department of Physics, Universität Hamburg, Jungiusstraße 9, 20355 Hamburg, Germany*

[10]*Institut für Physik, Universität Kassel, Heinrich-Plett-Straße 40, 34132 Kassel, Germany*

[11]*School of Chemistry, University of Southampton, Highfield, Southampton, SO17 1BJ, UK*

[12]*Max-Born-Institute, Max-Born-Straße 2A, 12489 Berlin, Germany*

[13]*J. R. Macdonald Laboratory, Department of Physics,*
Kansas State University, Manhattan, Kansas 66506, USA

[14]*Department of Chemistry and Biomolecular Sciences, University*
of Ottawa, 150 Louis Pasteur, Ottawa, Ontario, K1N 6N5, Canada

[15]*Ruhr-Universität Bochum, Fakultät für Chemie und Biochemie,*
Organische Chemie II, Universitätsstraße 150, 44801 Bochum, Germany

[16]*Department of Physics, University of Ottawa, 150*
Louis Pasteur, Ottawa, Ontario, K1N 6N5, Canada

[17]*NRC-uOttawa Joint Centre for Extreme Photonics, Ottawa, ON K1A 0R6, Canada*

[18]*Department of Chemistry, University of California, Davis, CA 95616, USA*

(Dated: December 4, 2025)

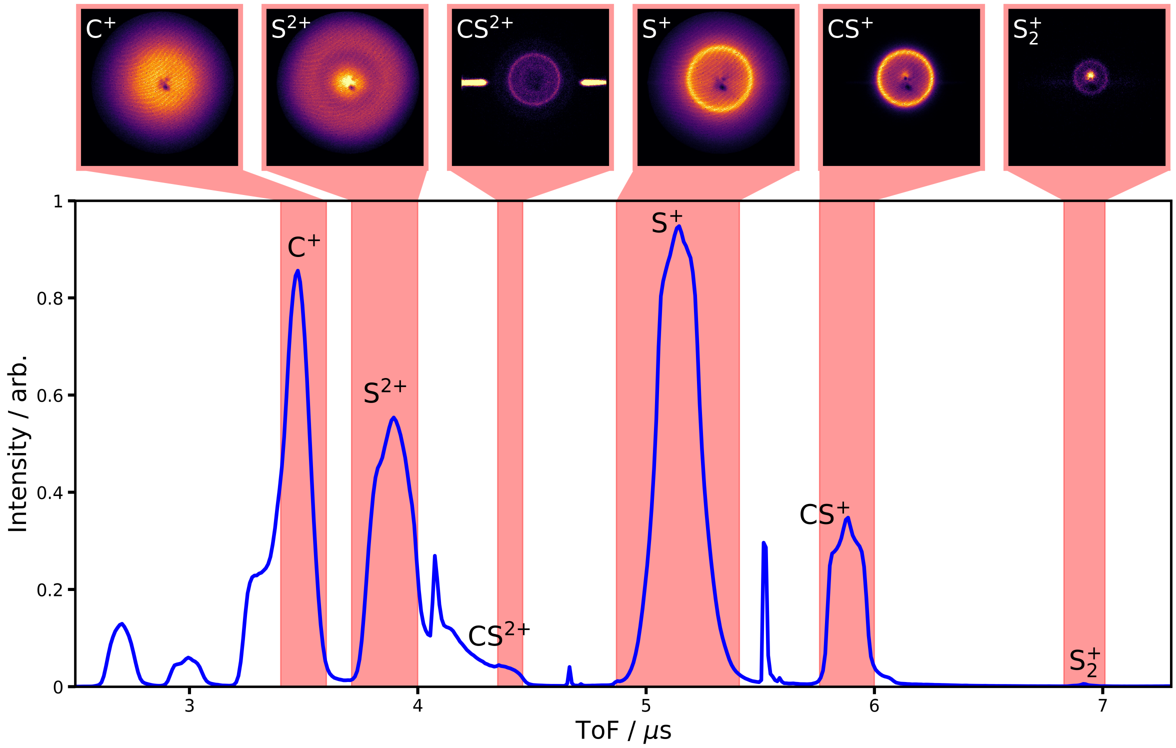

FIG. S1. Ion time-of-flight (ToF) spectrum observed following X-ray ionization of CS_2. The ion species analyzed in the main manuscript are labeled. Detector-plane images for each ion, obtained by integrating the Timepix3 camera data over the shaded ToF ranges, are also displayed. These ion images are plotted on separate colorscales.

S1. RAW ION IMAGING DATA

Figures S1 and S2 show representations of the 'raw' ion imaging data recorded by the Timepix3 camera, following hit finding and centroiding but prior to any covariance analysis. Figure S1 displays the ion time-of-flight (ToF) spectrum, as well as the detector-plane ion images for the ions that are analyzed in the current work, which are obtained by integrating the three-dimensional Timepix3 camera data over the ToF regions indicated. Figure S2 represents the same data as two-dimensional histograms (colloquially known as 'fish plots') of a) ToF and detector x position b) ToF and detector y position. We note that these plots show that the CS^{2+} ion overlaps heavily with background signal, primarily from ionization of background water in the chamber along the propagation axis of the X-ray beam (the x

---

† felix.allum@desy.de

‡ ruforbes@ucdavis.edu

axis of the detector), which leads to ‘lines’ in both the detector-plane images and the fish plots. Such signal is effectively removed in the covariance analysis and so does not present issues to the analysis presented in the main manuscript.

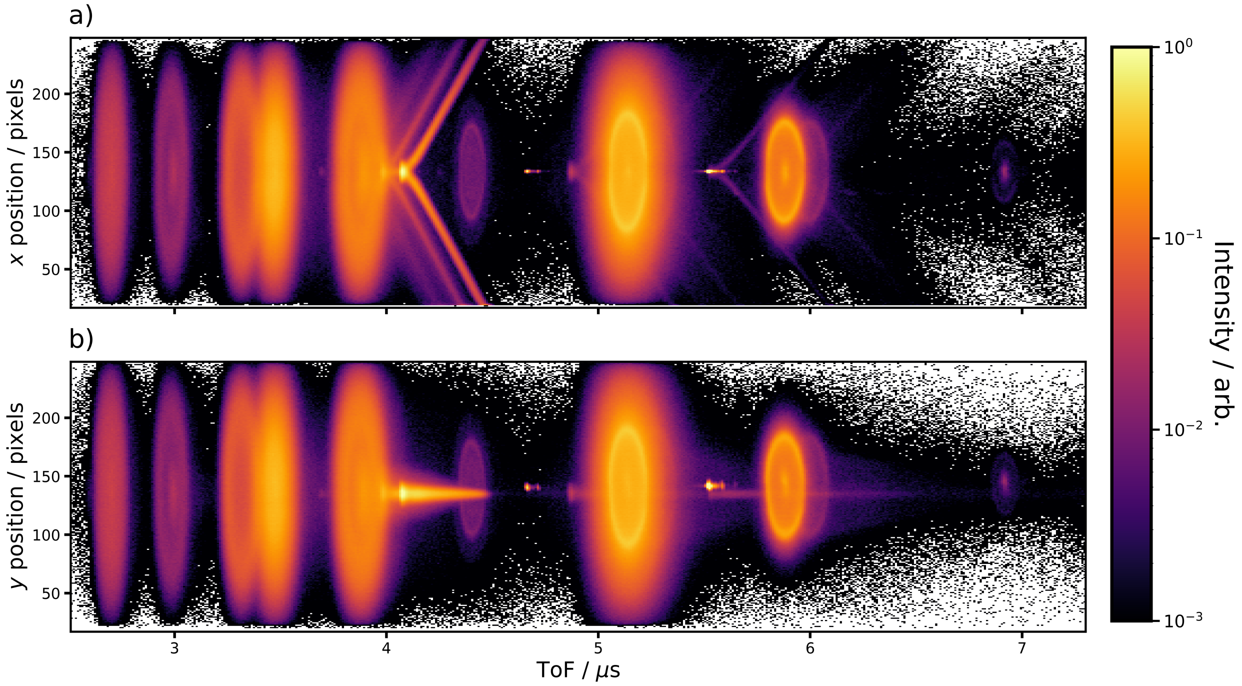

FIG. S2. Two-dimensional histograms of the Timepix3 camera VMI data, binned in a) ToF and detector x position b) ToF and detector y position. Data is plotted on a logarithmic colorscale, as indicated.

S2. WIGNER SAMPLING FOR COULOMB EXPLOSION SIMULATIONS

For the Coulomb explosion simulations shown in Figure 5, harmonic Wigner sampling was used to approximate the initial spread of atomic positions and momenta prior to Coulomb explosion. For this, the displacement and momentum along each normal mode were independently sampled [1–3]. For each simulation initial condition, the displacement Q and momentum P along a normal mode were randomly selected by sampling from the Wigner function. For a given P and Q, the unitless Wigner function is then evaluated as:

$$W(Q,P,n) = (-1)^n L_n(2R^2) e^{-R^2} \tag{1}$$

where $R^2 = Q^2 + P^2$, L_n is the nth Laguerre polynomial, and n is the vibrational quantum in the mode, which can be sampled from a Boltzmann distribution for a temperature T. As $L_n = 1$, the above expression simplifies considerably if only considering the case of T=0, where population is exclusively in $n = 0$. In practice, this sampling occurs by randomly selecting a value for P and Q, as well as a number m uniformly distributed between 0 and 1. If $W > m$, then the initial condition is selected. The dimensionless coordinates are then transferred into real ones and added to the initial three-dimensional position and velocity vector for each atom (in atomic units):

$$r(x, y, z) = r(x, y, z) + \frac{Q_i}{\sqrt{\omega_i}}\mathbf{i} \tag{2}$$

$$v(x, y, z) = v(x, y, z) + P_i\sqrt{\omega_i}\mathbf{i} \tag{3}$$

This is then repeated for each normal mode $\mathbf{i}$ in the molecule. In CS_2, there are four such modes: the symmetric stretch ($\omega_{ss} = 658\text{cm}^{-1}$), the asymmetric stretch ($\omega_{as} = 1535\text{cm}^{-1}$) and the doubly degenerate bend ($\omega_b = 397\text{cm}^{-1}$) [4].

S3. NATIVE FRAME ANALYSIS

As described in the main manuscript, native frames analysis [5, 6] is used to distinguish between sequential and concerted fragmentations, and to extract physical parameters related to any sequential dissociation channels. Here, we describe this analysis in detail, using the S^++ C+ S^+ channel as an example. If this fragmentation occurred sequentially, it would involve an initial fragmentation into S^++ CS^+, followed by secondary breakup of CS^+ into C+ S^+. We can define a conjugate momentum corresponding to the initial fragmentation into CS^+_{II}+S^+_{I} as:

$$\mathbf{p}_{\mathbf{CS^+_{II}},\mathbf{S^+_I}} = \frac{\mathrm{m_{CS}}}{\mathrm{m_{CS_2}}}\mathbf{p}_{\mathbf{S^+_I}} - \frac{\mathrm{m_S}}{\mathrm{m_{CS_2}}}(\mathbf{p}_{\mathbf{S^+_{II}}} + \mathbf{p}_{\mathbf{C}}) \tag{4}$$

where S^+_{I} and S^+_{II} distinguish the sulfur ions emitted from the first and second steps of the sequential fragmentation. A conjugated momentum associated with the secondary fragmentation of CS^+ can be similarly defined as:

$$\mathbf{p}_{\mathbf{CS}_{\mathbf{II}}^{+}} = \mu_{\mathrm{CS}} \left(\frac{\mathbf{p}_{\mathbf{S}_{\mathbf{II}}^{+}}}{\mathrm{m_S}} - \frac{\mathbf{p}_{\mathbf{C}}}{\mathrm{m_C}} \right) \tag{5}$$

where μ_{CS} is the reduced mass of CS^+. The KER associated with each step can be calculated from these conjugate momenta:

$$\mathrm{KER}_{\mathrm{CS}_{\mathrm{II}}^{+},\mathrm{S}_{\mathrm{I}}^{+}} = \frac{|\mathbf{p}_{\mathbf{CS}_{\mathbf{II}}^{+},\mathbf{S}_{\mathbf{I}}^{+}}|^2}{2\mu_{\mathrm{CS,S}}} \tag{6}$$

$$\mathrm{KER}_{\mathrm{CS}_{\mathrm{II}}^{+}} = \frac{|\mathbf{p}_{\mathbf{CS}_{\mathbf{II}}^{+}}|^2}{2\mu_{\mathrm{CS}}} \tag{7}$$

Similarly, we can compute the angle between the two dissociation vectors as:

$$\theta_{\mathrm{CS}_{\mathrm{II}}^{+},\mathrm{S}_{\mathrm{I}}^{+}} = \cos^{-1} \left(\frac{\mathbf{p}_{\mathbf{CS}_{\mathbf{II}}^{+}} \cdot \mathbf{p}_{\mathbf{CS}_{\mathbf{II}}^{+},\mathbf{S}_{\mathbf{I}}^{+}}}{|\mathbf{p}_{\mathbf{CS}_{\mathbf{II}}^{+}}||\mathbf{p}_{\mathbf{CS}_{\mathbf{II}}^{+},\mathbf{S}_{\mathbf{I}}^{+}}|} \right) \tag{8}$$

S4. INFLUENCE OF 200 NM LASER

As mentioned in the main text, the data analyzed in the current work was taken from a 200 nm pump – X-ray probe study [7, 8]. As the present work is concerned solely with dynamics induced by the X-ray pulse, data was filtered by pump-probe delay to select data where pump-probe delays of less than -100 fs (i.e. where the X-ray pulse precedes the UV pulse by at least 100 fs). Consequently, in the selected data, X-ray ionization only occurs on unpumped molecules.

Figures S3 and S4 show example time-of-flight spectra and selected ion momentum distributions for: X-ray only, 200 nm-only, and 200 nm + X-ray (delays less than -100 fs, i.e. X-ray early). Firstly, it can be seen that the primary ion produced by the 200 nm pulse is the CS_2^+ parent. It should be noted that as CS_2^+ ions are produced with very low velocity, mapping to a small central region of the detector, this signal is prone to saturation. A small quantity of low momentum S^+ and CS^+ ions are also produced from dissociative ionization,

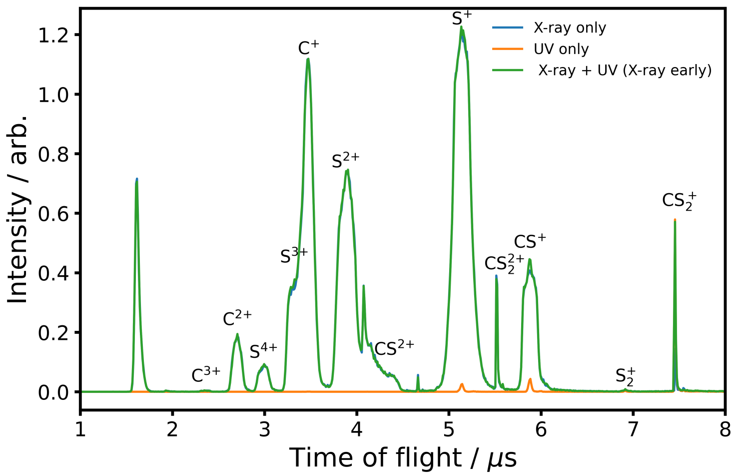

FIG. S3. Comparison of time-of-flight spectra for: X-ray only (blue), 200 nm only (orange), and X-ray + 200 nm (X-ray early) (green). Each spectrum is normalized to the total number of acquisition cycles (laser/FEL shots).

with no evidence of Coulomb explosion. The post-ionization of fragments produced by X-ray ionization is seen as extremely unlikely due to the low intensity of the 200 nm pulse, which is able to two-photon ionize CS_2^+ primarily due to the extremely large absorption cross-section of neutral CS_2 at 200 nm (several hundred Mbarn [9]). The similarity of the time-of-flight and ion momentum distributions for X-ray only and 200 nm + X-ray (X-ray early) data supports this claim, and thus the validity of using the 200 nm + X-ray (X-ray early) data in the present work.

S5. THE S^++ C^++ S^+ CHANNEL

Figures S5 and S6 show alternative representations of the (S^+, C^+, S^+) three-fold covariance. The first of these, S5, is a 'Dalitz' plot [10], as is frequently used to kinematically analyze fragmentation processes, including in previous work on CS_2 [11, 12] and the closely-related CO_2 [13–16]. For a more detailed discussion of Dalitz plots, and their interpretation in the context of triatomic fragmentation dynamics, the reader is directed to these past studies. In the present work, to construct a covariance Dalitz plot, covariance intensity is histogrammed according to the following x and y coordinates:

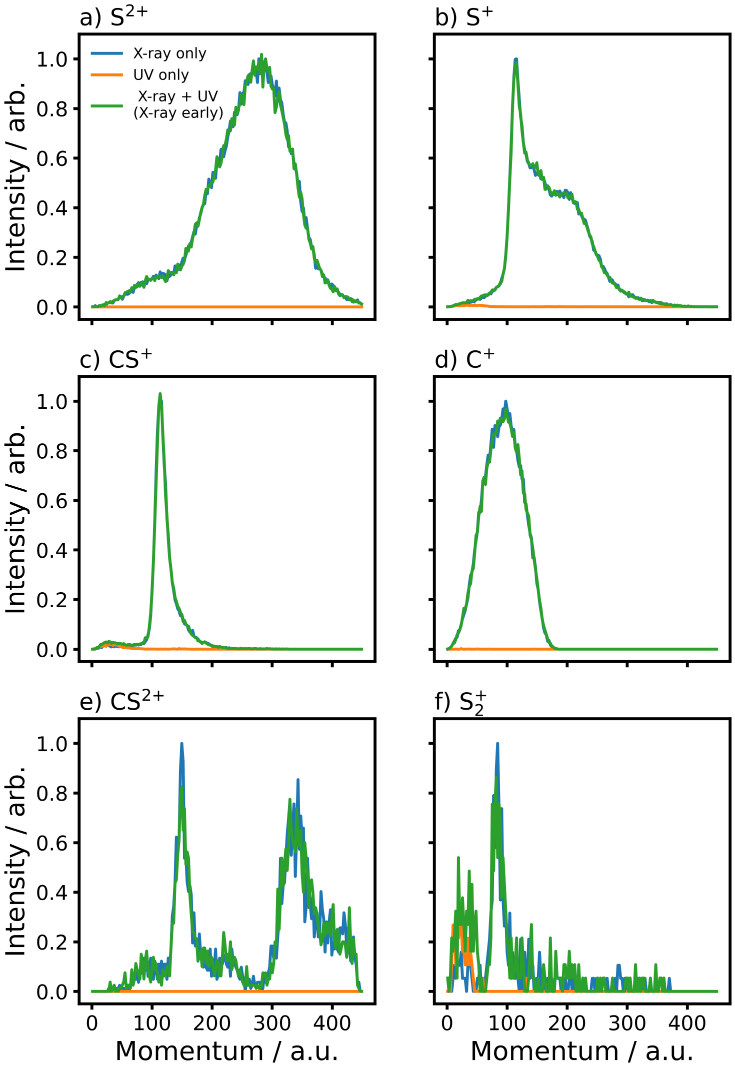

FIG. S4. Comparison of ion momentum distributions (in atomic units) for: X-ray only (blue), 200 nm only (orange) and X-ray + 200 nm (X-ray early) (green). Each momentum distribution is normalized to the total number of acquisition cycles (laser/FEL shots).

$$x = \frac{\mathrm{KE}_{\mathrm{S}_1^+} - \mathrm{KE}_{\mathrm{S}_2^+}}{\sqrt{3}\mathrm{KER}} \tag{9}$$

$$y = \frac{\mathrm{KE}_{\mathrm{C}^+}}{\mathrm{KER}} - \frac{1}{3} \tag{10}$$

where $\mathrm{KE}_{\mathrm{S}_1^+}$, $\mathrm{KE}_{\mathrm{S}_2^+}$, $\mathrm{KE}_{\mathrm{C}^+}$ and KER are the KE of the first S^+ ion, the KE of the second S^+ ion, the KE of the C^+ ion and the total KER, respectively. In this case, the two S^+

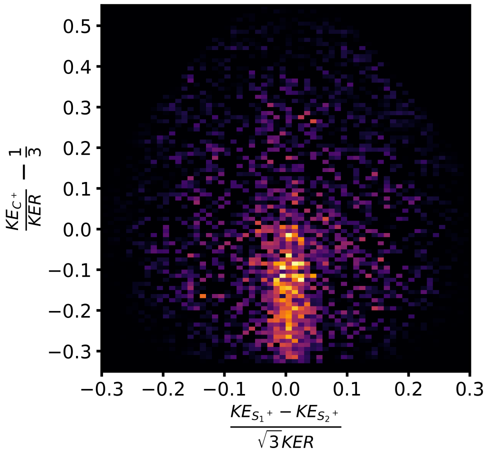

FIG. S5. Dalitz plot representation of the (S^+, C^+, S^+) three-fold covariance.

ions are indistinguishable and so the distribution is symmetric about 0 in x. Qualitatively, the Dalitz plot is very similar in appearance to that reported by Wang *et al.* [11] from a study using electron impact ionization. The localization of intensity in this representation arises from the dominance of concerted fragmentation, while the extent of the feature in y represents the importance of fragmentation of bent geometries, in which the C^+ ion can receive considerable KE. The main discrepancy between the Dalitz plot shown in Fig. S5 and that reported by by Wang *et al.* [11] is the lack in the current work of weak signal associated with sequential fragmentation, which manifests as signal distributed along diagonal lines. As discussed in the main text, this may be due to sequential fragmentation being less prominent under our experimental conditions and/or not being observable above the noise floor of our measurement.

The lack of sequential fragmentation in the S^++ C^++ S^+ channel in our data is further corroborated by native frames analysis, which was described in some detail in the main manuscript and in Section S3 of this Supplementary Material. Figure S6 shows the three-fold (S^+, C^+, S^+) covariance in the analogous native frame representation to that used in Fig. 7 of the main manuscript (for the S^++ C+ S^+ channel). Signal is relatively well-localized in θ, as expected for a concerted breakup. There is no discernible signal spanning a wide range of θ angles, as would be expected for a sequential fragmentation via a long-lived CS_2^+ intermediate.

Figure 4 presented example simulations for 'asynchronous' and 'sequential' breakups into

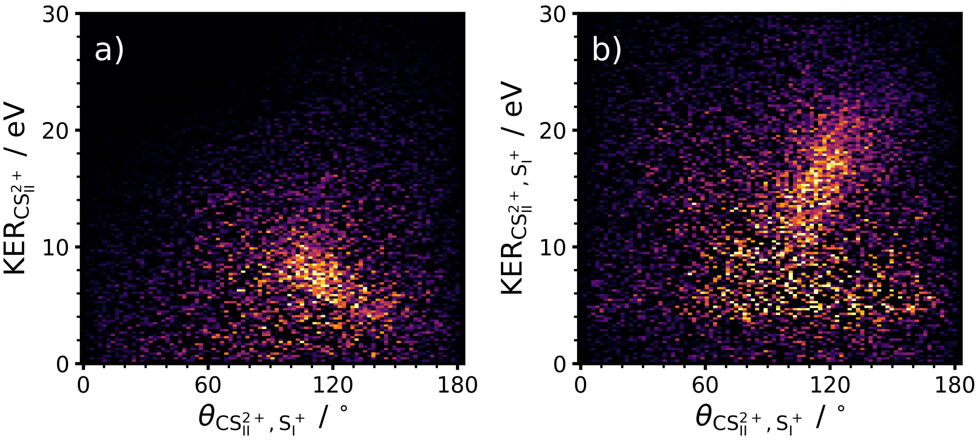

FIG. S6. Three-fold (S^+, C^+, S^+) native frame covariance analysis.

$S^+ + C^+ + S^+$. These were produced by classically simulating a two-step Coulomb explosion, in which CS_2^{3+} firstly fragments into S^+ and CS^{2+}, with the latter then exploding at a later time. In this modeling, the dissociation lifetime, τ, and the rotational period τ_R, of the CS^{2+} may be varied. Figure S7 compares the simulated Newton plots for a range of parameters for these values. These are compared to the equivalent plot assuming a completely concerted fragmentation of a Wigner sampled pool of geometries, shown in panel a).

S6. THE S^++C+S^+AND S^++C^++S CHANNELS

As discussed in the main manuscript, the native frames analysis for the S^++ C+ S^+ channel is complicated somewhat by the fact that the two S^+ ions cannot be distinguished in our analysis, although for a sequential fragmentation the two are distinct (with one being emitted in each step of the sequential fragmentation). The misassignment of S_{I}^+ and S_{II}^+ leads to signal in Fig. 7 spanning a wide range of $\mathrm{KER}_{\mathrm{CS}_{\mathrm{II}}^+}$ focussed at $\theta_{\mathrm{CS}_{\mathrm{II}}^+,\mathrm{S}_{\mathrm{I}}^+}$ close to 180 degrees. This can be confirmed in the analysis of the sequential fragmentation simulations where, unlike in the experiment, we can unambigiously distinguish the two S^+ ions. This is shown in Fig. S8. Panels a) and b) show the same native frames analysis as in Fig. 7 in the main manuscript while panels c) and d) show the same analysis in which the two S^+ ions are distinguished, and correctly assigned to S_{I}^+ and S_{II}^+. As can be seen, in this case only the signal with low $\mathrm{KER}_{\mathrm{CS}_{\mathrm{II}}^+}$ spanning all $\theta_{\mathrm{CS}_{\mathrm{II}}^+,\mathrm{S}_{\mathrm{I}}^+}$ remains, confirming that this signal comes from sequential fragmentations in which S_{I}^+ and S_{II}^+ are correctly assigned.

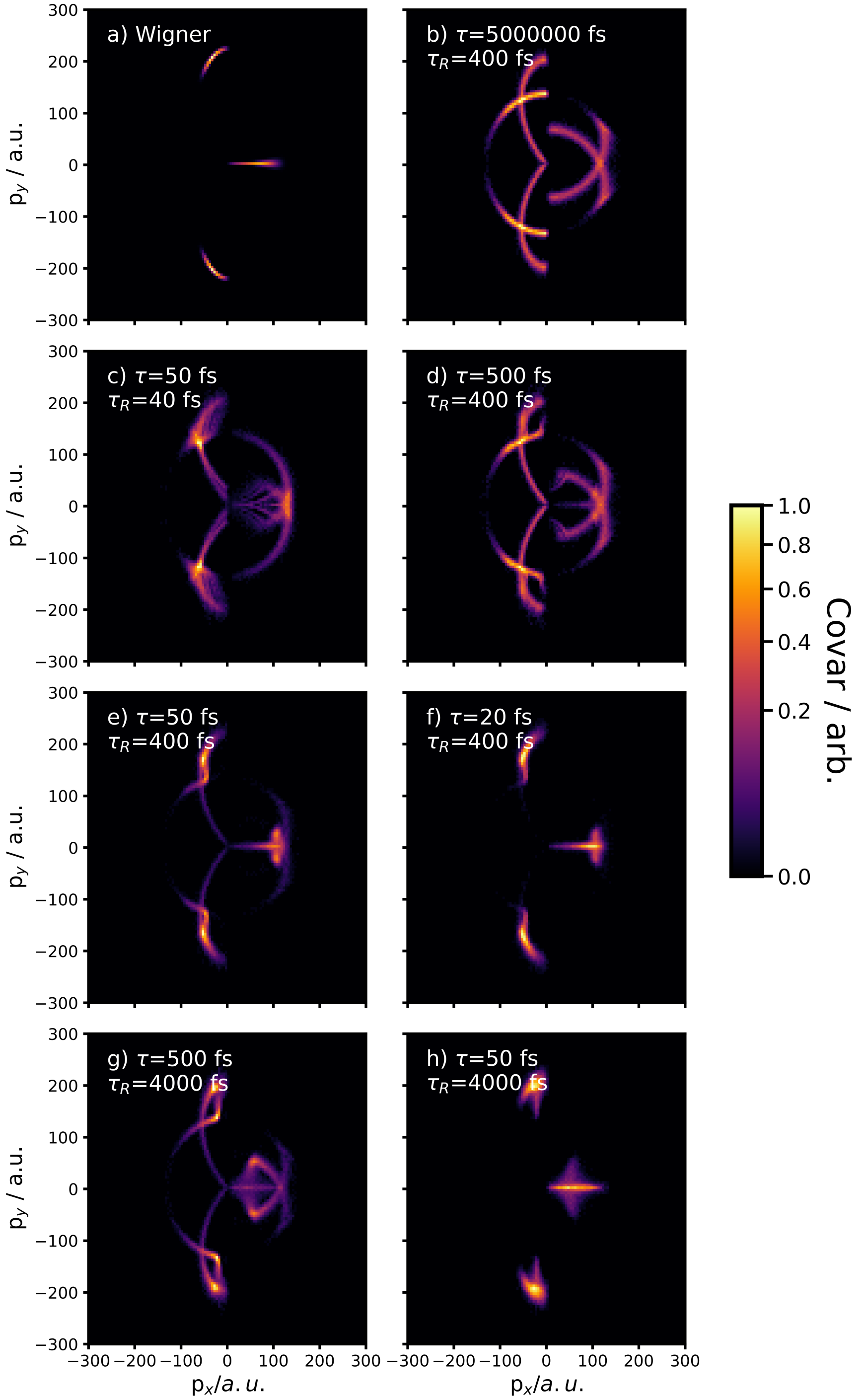

FIG. S7. Newton plot representations of the relative ion momenta from different simulations of the S^++ C^++ S^+ channel. Panel a) corresponds to simulation for concerted fragmentation of a Wigner-sampled pool of initial atomic positions and momenta, whilst panels b) to h) correspond to sequential/asynchronous simulations with different parameters, as labeled and discussed in the text.

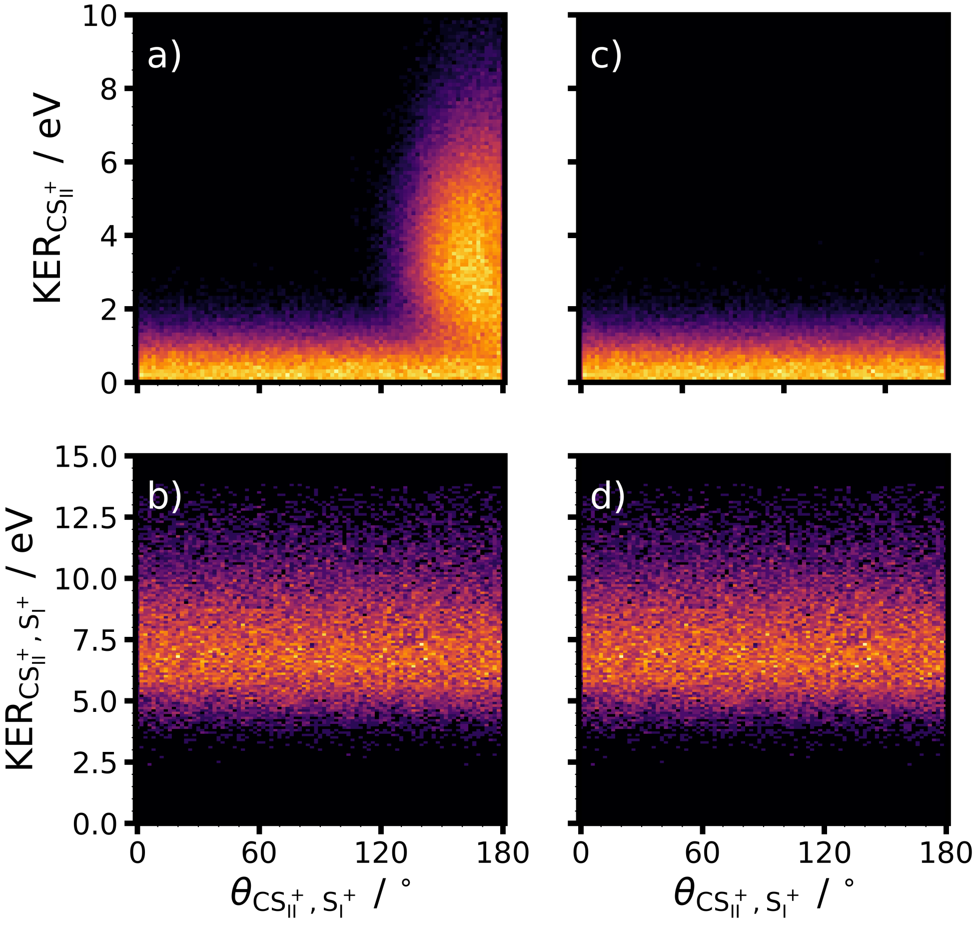

FIG. S8. Native frame analaysis for the sequential simulations of the S^+ + C + S^+ channel. In panels a) and b), the two S^+ are not distinguished in the analysis (as in analysis of the experimental data), while in panels c) and d), only the correct assignment of S_I^+ and S_{II}^+ is made.

In the experimental native frames analysis of the S^++ C+ S^+ channel, there is also an excess of signal at low (∼0-3 eV) $KER_{CS_{II}^+}$ with $\theta_{CS_{II}^+, S_I^+} > \sim 120°$, which is not reproduced in the simulations of the sequential fragmentation. This signal can be assigned to concerted fragmentations. To support this, we performed a simple simulation of concerted fragmentation into the S^++ C+ S^+ channel. Here, a ground-state distribution of atomic positions and momenta was sampled from a Wigner distribution, and a prompt, classical Coulomb explosion was simulated in which the two S atoms had a charge of +1, while the C atom had a charge of +0.1. Figure S9b) shows the outputs from this simulation plotted in the native frame, compared to the equivalent plot from experimental data in panel a). It can be seen that qualitatively, the concerted simulation spans the same region as the previously-

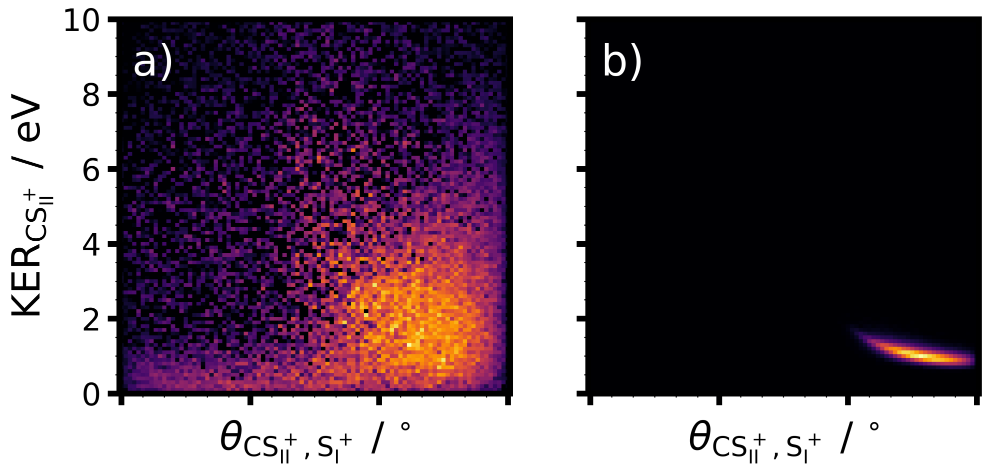

FIG. S9. Comparison of (S^+, S^+) native frames covariance analysis of a) the experimental data and b) the simple simulation of a concerted S^++ C+ S^+ fragmentation.

identified experimental signal, particularly in terms of the range of $\theta_{CS_{II}^+,S_I^+}$. It is unsurprising that this simple simulation, in which the C atom is given a fixed charge of +0.1, substantially underestimates the span of the true KER distribution associated with concerted S^++ C+ S^+ fragmentation. Much like the case of the S^++ C^++ S^+ discussed in the main text (Fig. 5), multiple factors not included in this simple modeling broaden the kinetic energy distribution of this feature.

Figures S10 and S11 compare the output of the experimental (S^+, S^+) two-fold covariance in the β-KER representations (used in Fig. 6 of the main manuscript) to that produced by the sequential and concerted simulations of the S^++C+S^+ fragmentation. While both channels produce signal with a β (S^+, S^+) close to 180°, the β (S^+, C) distribution is rather different in the two cases. The concerted fragmentation produces a β (S^+, C) of around 100 °, while the signal from sequential fragmentation is concentrated towards both smaller and greater values of β (S^+, C).

In order to explore the role of sequential fragmentation in the S^++ C^++ S channel, we again turn to native frames analysis of the (S^+, C^+) covariance. Results are shown in Figure S12. Unlike the S^++ C+ S^+ case, there are now two possible sequential fragmentation pathways that can contribute. A neutral S may be emitted in the primary dissociation to yield CS^{2+} which then dissociates on a longer timescale. Alternatively, a S^+ ion is initially

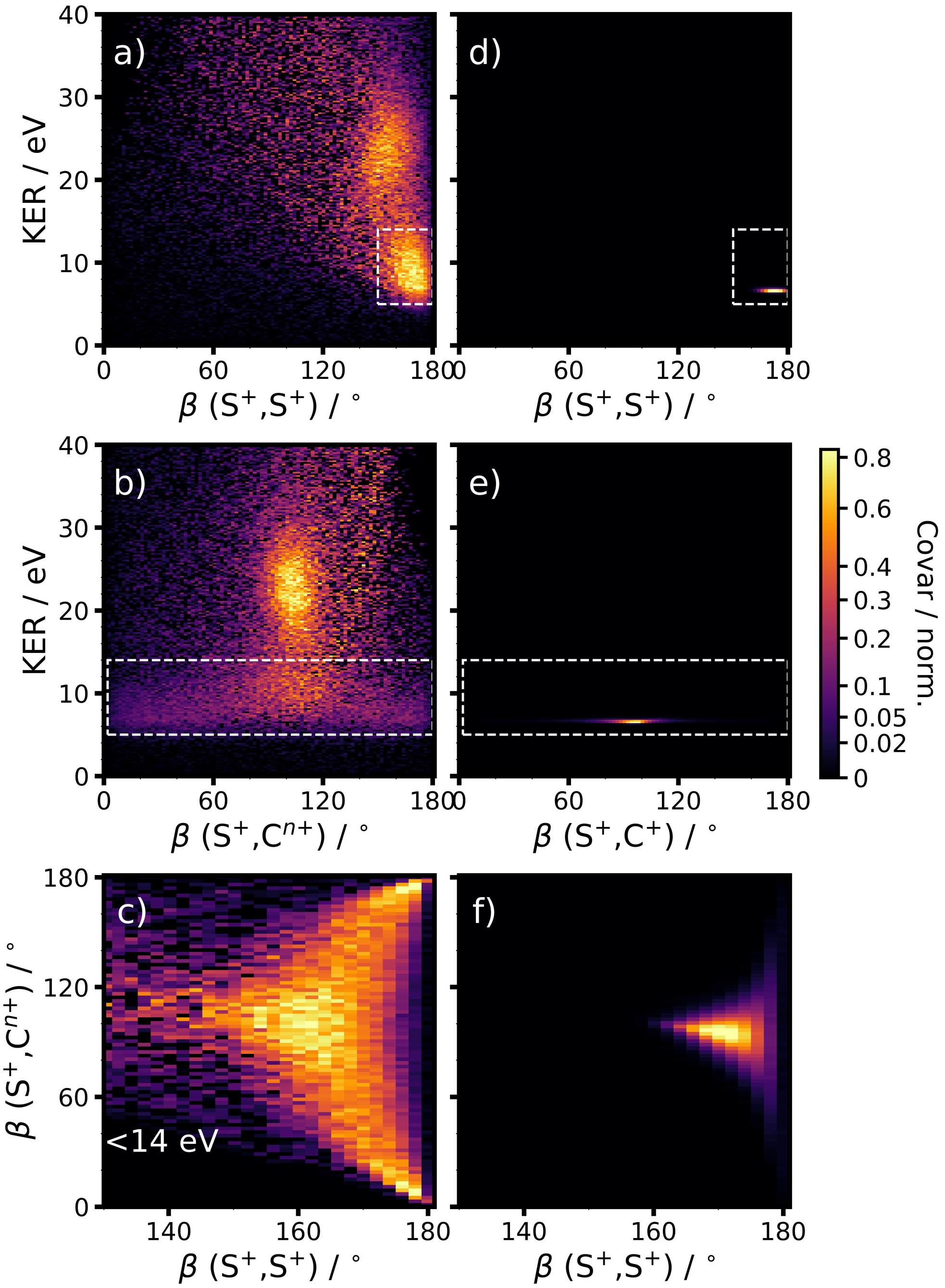

FIG. S10. Comparison between the β-KER representations of the a)-c) experimental (S^+, S^+) covariance and the d)-f) simulated (S^+, S^+) covariance for concerted fragmentation.

eliminated to produce a CS^+ which then undergoes secondary fragmentation. However, when the data is analyzed in the native frame for either sequential fragmentation scenario, we do not observe a feature that uniformly spans all angles, and so we do not believe that sequential fragmentation by a long-lived intermediate contributes significantly to the S^++

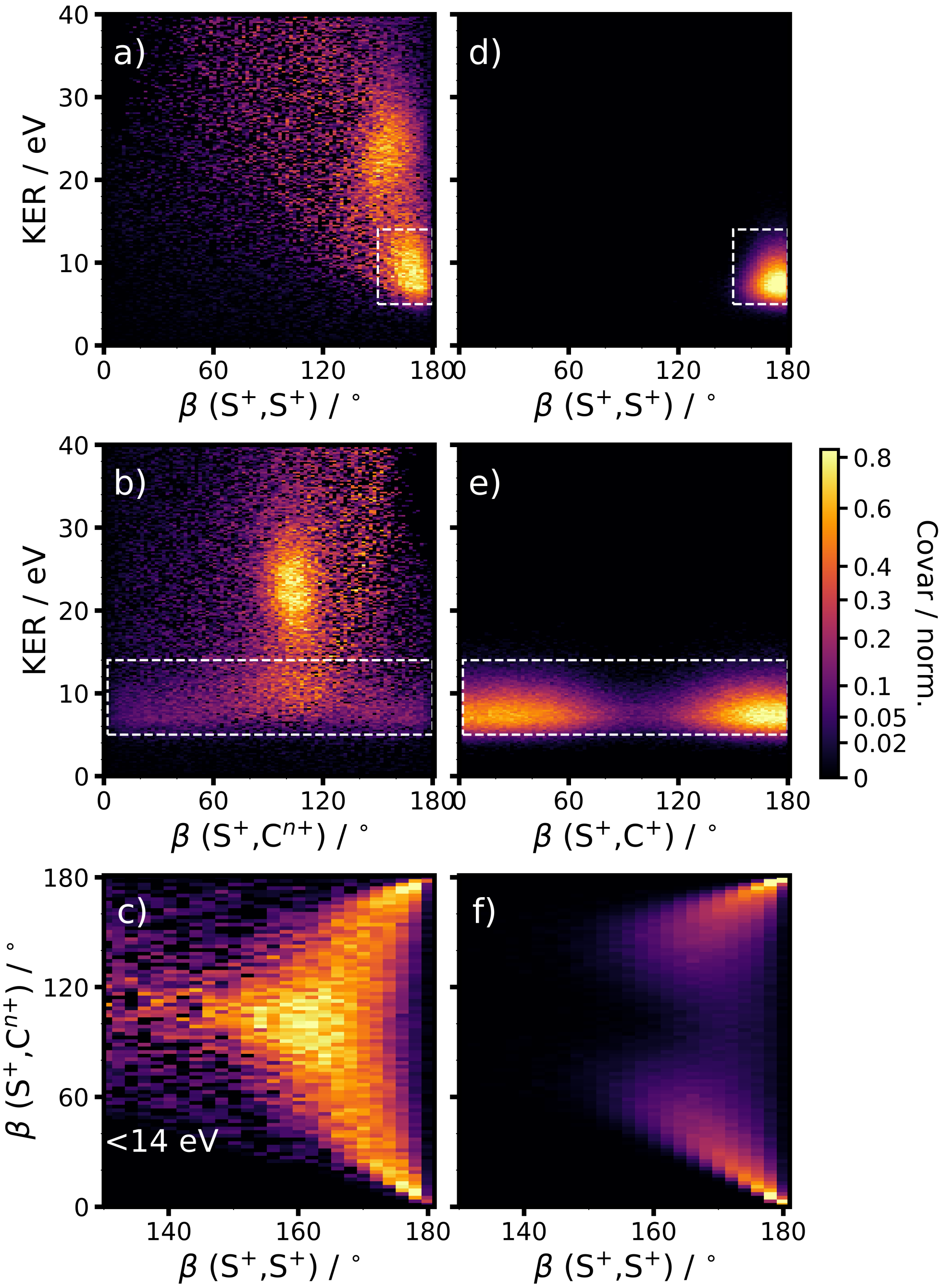

FIG. S11. Comparison between the β-KER representations of the a)-c) experimental (S^+, S^+) covariance and the d)-f) simulated (S^+, S^+) covariance for sequential fragmentation.

C^++ S channel.

Figure S13 shows the two-fold (S^+, S^+) and (S^+, C^+) covariances represented as Dalitz plots, as described above. In both cases, only events with a total KER of less than 14 eV

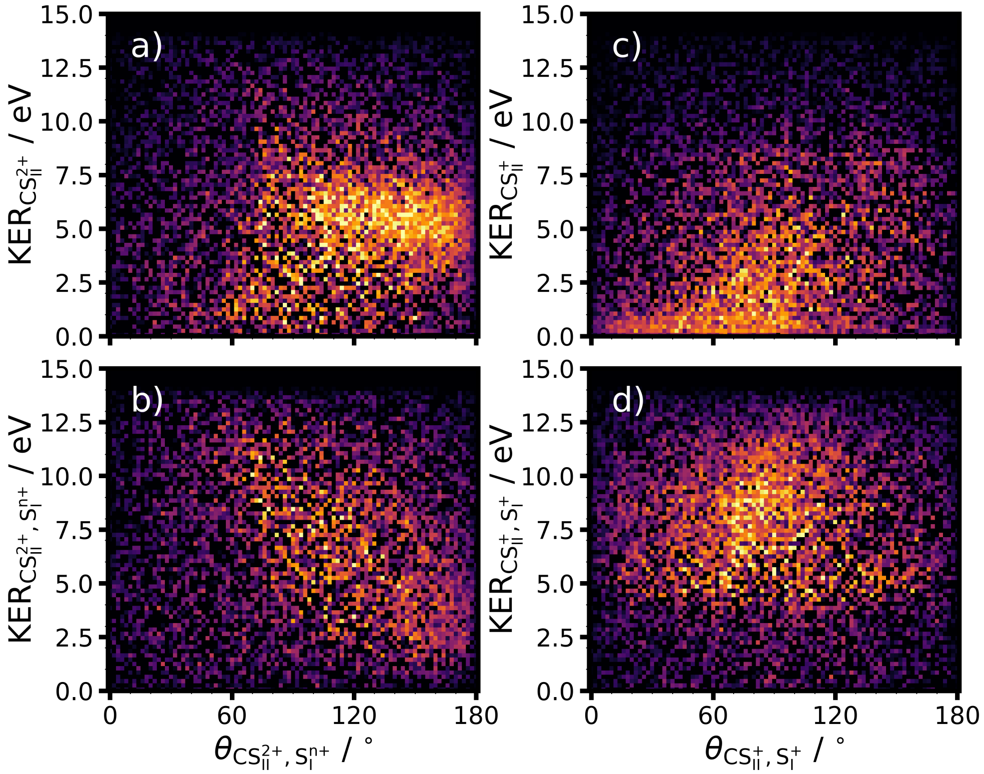

FIG. S12. Native frame (S^+, C^+) covariance analysis, for total KERs of less than 12 eV, to isolate S^++ C^++ S signal. Panels a) and b) assume a CS^{2+} intermediate, whilst panels c) and d) assume a CS^+ intermediate, as discussed in the text.

were plotted, to reject signal from three-body S^++ C^++ S^+ fragmentation. In the case of the (S^+, C^+), the two sulfurs can be distinguished, as one is detected as an S^+ ion (S_1), while the momentum of the other is determined through momentum conservation, and assumed to be neutral (S_2). Immediately, rather different signals are observed to that associated with the S^++ C^++ S^+ channel (Fig. S5). These plots may also be compared with analogous plots determined from coincidence analysis following S 2p ionization reported by Saha *et al.* [12] (in particular, as shown in Fig. 6 of Saha *et al.*, which separates events based on total KER in a similar way to our current analysis).

S7. THE S^{2+}+ C+ S^+AND S^{2+}+ C^+ +S CHANNELS

Figure S14 compares the two-fold (S^{2+}, C^+) and three-fold (S^{2+}, C^+, C^+) covariances. Low KER signal which is highlighted by the box in panels a) and b) is present in the former

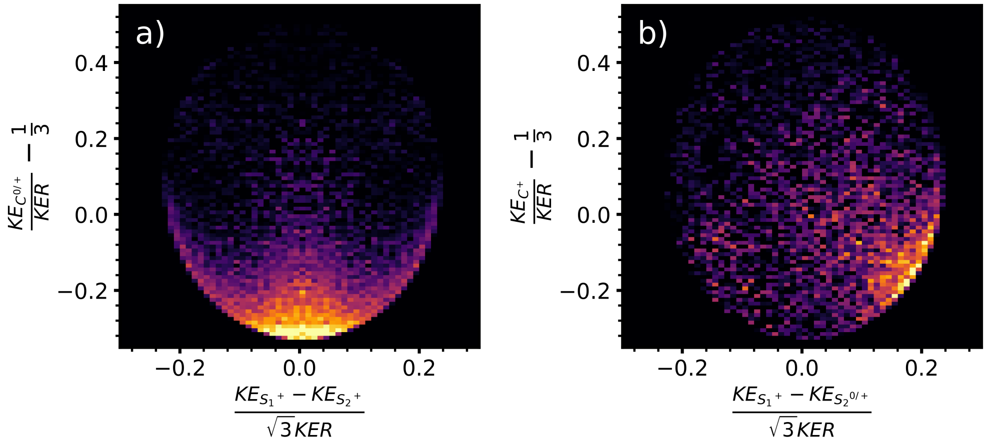

FIG. S13. Dalitz plot representations of the (S^+, S^+) (a) and (S^+, C^+) (b) covariances. In both cases, events with a total KER of less than 14 eV are analysed, to remove contributions from the S^++ C^++ S^+ channel.

but not the latter, and thus is assigned to trication Coulomb explosion into S^{2+}+ C^++ S.

For both the three-body fragmentation channels originating from the trication which yield a neutral fragment (i.e. S^{2+}+ C+ S^+ and S^{2+}+ C^++ S), native frames analysis of the relevant two-fold covariances was used to assess the role of sequential fragmentation. Figure S15 presents results from this analysis for the S^{2+}+ C+ S^+ channel, using (S^{2+}, S^+) covariance analysis. Here, only fragmentations with a total KER of less than 24 eV were included, to avoid contribution of fragmentation from CS_2^{4+}. If such a fragmentation were to occur sequential, it could in principle occur through either CS^+ or CS^{2+} intermediates, formed through the primary ejection of S^{2+} or S^+, respectively. Native frames analysis was performed for both these possibilities, with the assumption of a CS^+ intermediate plotted in panels a)-b) and a CS^{2+} intermediate plotted in panels c)-d). In both cases, however, there are no features that span all relative angles between the primary and secondary dissociations. As such, we conclude that sequential dissociation via a long-lived CS^+ or CS^{2+} intermediate does not significantly contribute to the S^{2+}+ C+ S^+ channel.

Figure S16 presents results from the analogous analysis for the S^{2+}+ C^++ S channel, from (S^{2+}, C^+) covariance analysis. For completeness, the analysis was repeated for the different possible sequential pathways contributing to this channel: via a CS^{3+} intermediate or a CS^+ intermediate. Although the signal-to-noise ratio for these covariances is rather poor, again

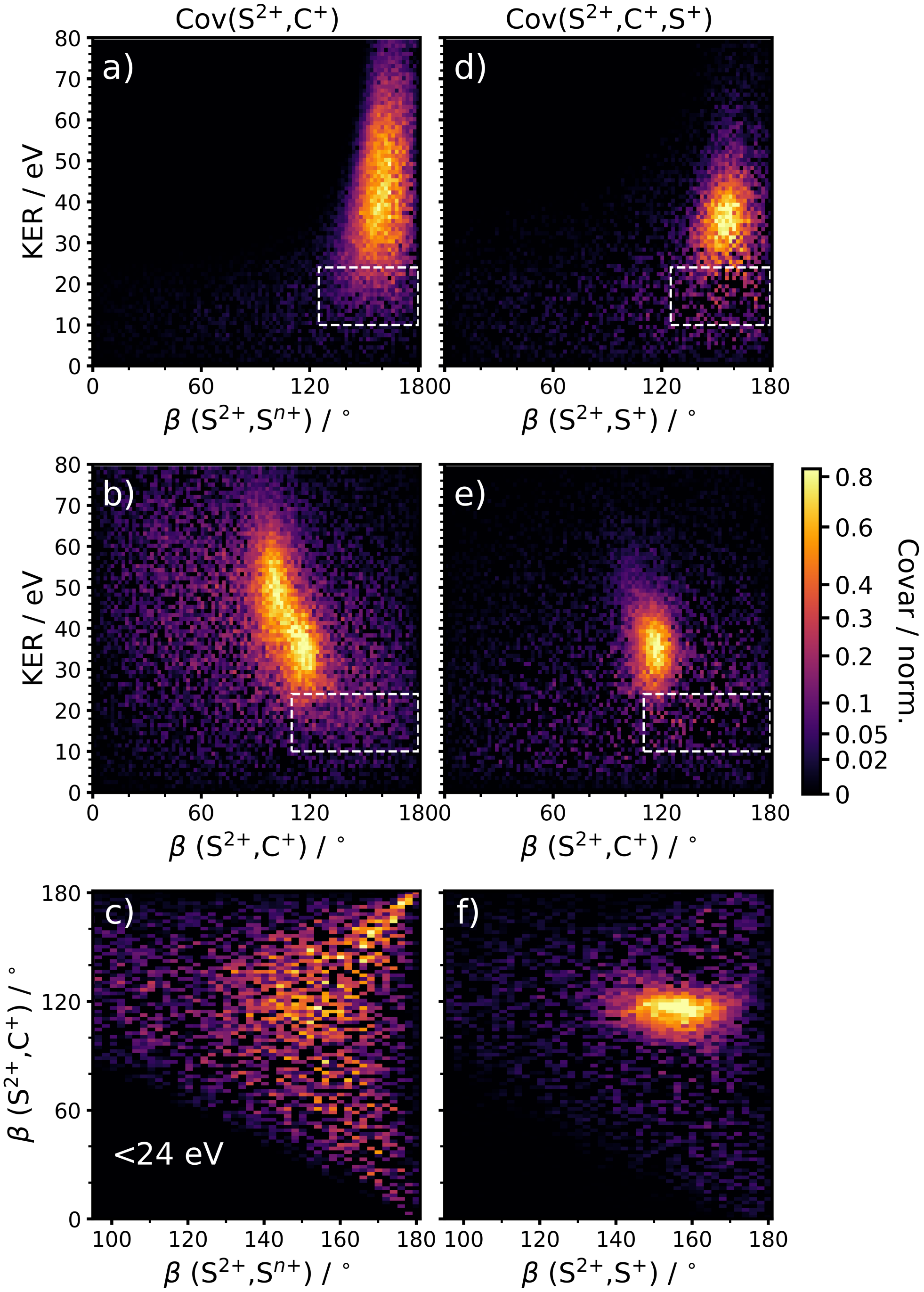

FIG. S14. Two-fold (S^{2+}, C^{+}) covariance, experimental (a) to c)), and three-fold (S^{2+}, C^{+}, S^{+}) covariance (d) to f)). Correlations are shown between: the total KER, the (S^{2+}, S^{n+}) recoil angle and (S^{2+}, C^{+}) recoil angle. In the two-fold covariance, the momentum of the third particle (S^{n+}) is inferred from momentum conservation, whilst in the three-fold case, the S^{+} momentum is recorded directly. In panel c), signal is only plotted for total KERs less than 24 eV, to isolate signal from the trication fragmentation channel, which is highlighted with a white box in other panels. As discussed in the text, such signal is absent in the three-fold covariance.

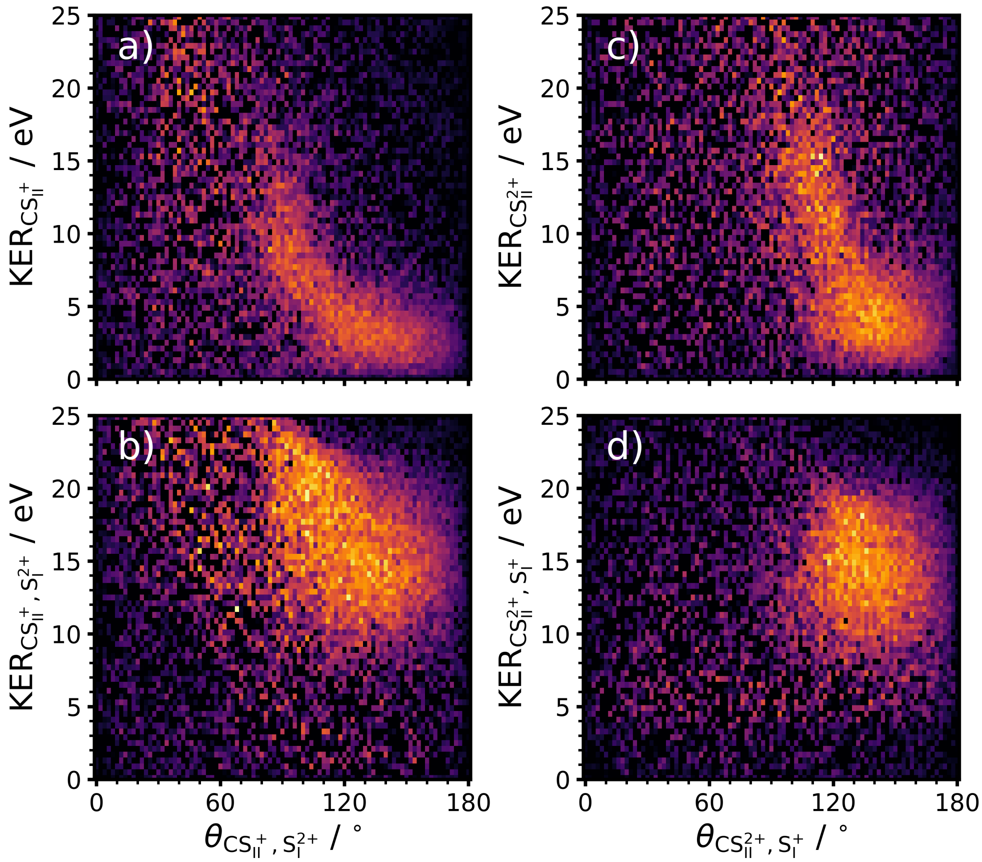

FIG. S15. Native frame (S^{2+}, S^{+}) covariance analysis, for total KERs of less than 24 eV, to isolate S^{2+}+ C+ S^{+} signal. Panels a) and b) assume a CS^{+} intermediate, whilst panels c) and d) assume a CS^{2+} intermediate, as discussed in the text.

we can identify no signal consistent with fragmentation via a long-lived intermediate, and conclude that this is not a major contributing pathway.

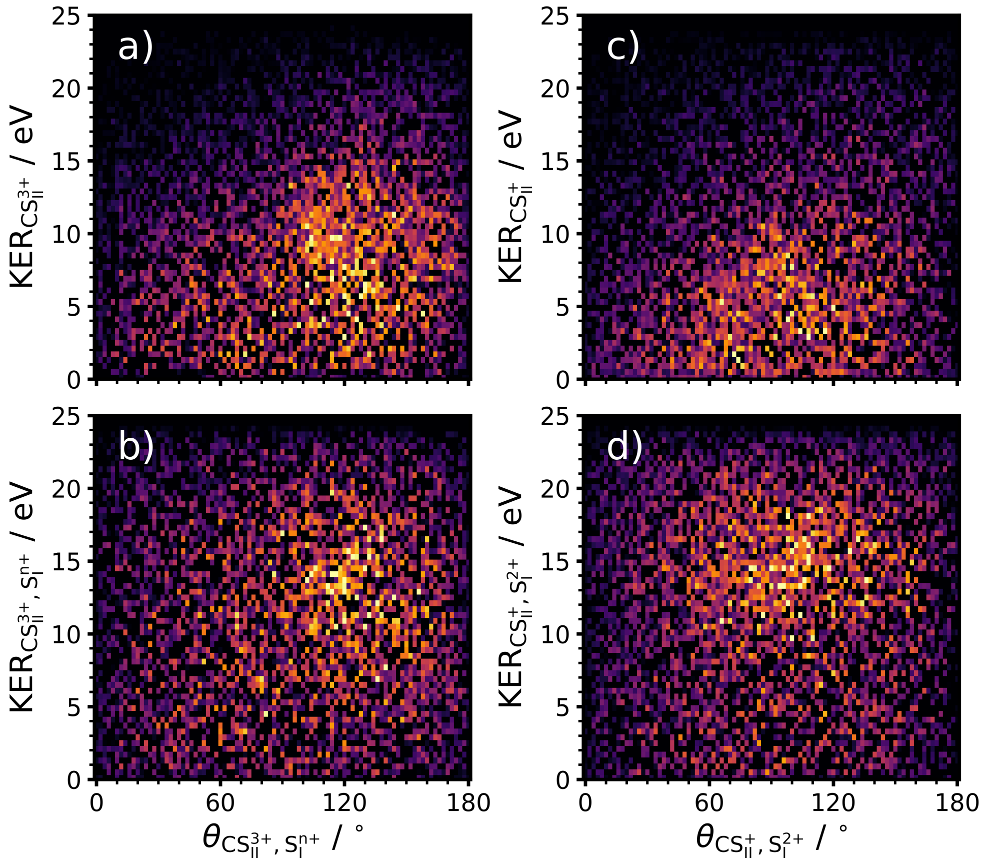

FIG. S16. Native frame (S^{2+}, C^{+}) covariance analysis, for total KERs of less than 24 eV, to isolate S^{2+}+ C^{+}+ S signal. Panels a) and b) assume a CS^{3+} intermediate, whilst panels c) and d) assume a CS^{+} intermediate, as discussed in the text.

S8. MEAN KER FOR OBSERVED FRAGMENTATION CHANNELS

From the analysis presented in Section III D of the main manuscript, mean KERs for three-body fragmentation channels with a neutral product fragment can be estimated. Mean KERs for the observed two-body fragmentation channels and the S^{+}+ C^{+}+ S^{+} channel can be directly extracted from the relevant two- and three-fold covariances. The mean KERs extracted for each fragmentation channel analyzed in the current work are summarized in Table S1.

Dication	
Channel	Mean KER (eV)
$S^{+} + C + S^{+}$	12.2
$S^{+} + C^{+} + S$	14.4
$S^{+} + CS^{+}$	6.00
$S_2^{+} + C^{+}$	5.46
Trication	
$S^{+} + C^{+} + S^{+}$	24.9
$S^{2+} + C + S^{+}$	20.8
$S^{+} + CS^{2+}$	10.2
$S^{2+} + CS^{+}$	11.9
$S^{2+} + C^{+} + S$	23.4

TABLE S1. Mean KER extracted for each analyzed fragmentation channel.

S9. POWER DEPENDENCE OF COVARIANCE SIGNALS

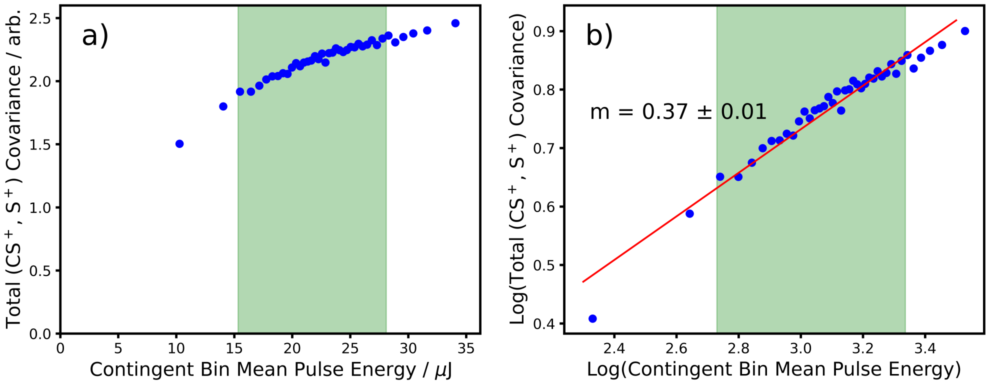

FIG. S17. Power dependence of the two-fold (CS^{+}, S^{+}) covariance. a) Total covariance intensity as a function of the mean X-ray pulse energy within each contingent bin. b) Log-log plot of the logarithm of covariance intensity verses the logarithm of X-ray pulse energy. A linear fit (red line) to these data, alongside the extracted gradient, m, is shown. In both a) and b), the pulse energy region used in the main data analysis throughout the manuscript is highlighted in green.

To further examine the possible role of multiphoton processes in the fragmentation processes studied, additional analysis exploring the power-dependence of the observed covariance signals was performed. This was done using the single-shot measurements of the incident X-ray pulse energies from the FLASH Gas Monitor Detector (GMD)[17]. As for all covariances present throughout the work, covariances were calculated in a contingent manner, by binning the data by incident pulse energy in equal-statistic bins. For the analysis presented in this section, contingent covariance analysis was performed with an increased number of contingent bins (40) over a greater range of incident pulse energies (4.3 μJ to 38.3 μJ).

Figure S17 presents such analysis for the two-fold (CS^+, S^+) covariance, which can be assumed produced following single-photon S 2p photoionization and subsequent AM decay. The total covariance, which is proportional to the number of $\mathrm{CS}^+ + \mathrm{S}^+$ fragmentation events detected per shot, increases with incident X-ray pulse energy, as expected. As highlighted in the log-log plot shown in panel b), the power dependence of the signal is not linear, with a gradient in the log-log plot of 0.37 ± 0.01. This indicates a significant saturation of this single-photon channel under the present experimental conditions.

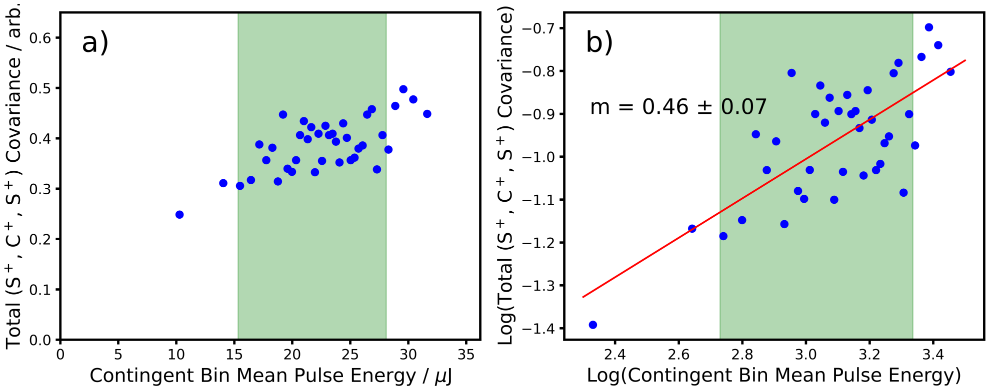

FIG. S18. Power dependence of the three-fold (S^+, C^+, S^+) covariance. a) Total covariance intensity as a function of the mean X-ray pulse energy within each contingent bin. b) Log-log plot of the logarithm of covariance intensity verses the logarithm of X-ray pulse energy. A linear fit (red line) to these data, alongside the extracted gradient, m, is shown. In both a) and b), the pulse energy region used in the main data analysis throughout the manuscript is highlighted in green.

Figure S18 presents the analogous analysis for the trication $\mathrm{S}^+ + \mathrm{C}^+ + \mathrm{S}^+$ fragmentation channel, from the three-fold (S^+, C^+, S^+) covariance. While here the data is slightly less clear, owing to the lower signal-to-noise ratio of the three-fold covariance, qualitatively similar power dependence is seen. A gradient in the log-log plot of 0.46 ± 0.07 is extracted. While this is slightly higher than that observed for the dication channel, it is difficult to conclude the statistical significance of this. From this analysis, however, we can be confident that both these channels are dominated by single-photon interactions (in the trication channel, a S 2p photoionization followed by two AM decays). While we cannot conclusively rule out contributions from a two-photon interaction to trication production (i.e. valence ionization of CS_2^{2+} dications formed by a single S 2p ionization), it does not appear to be a major contribution to the channel.

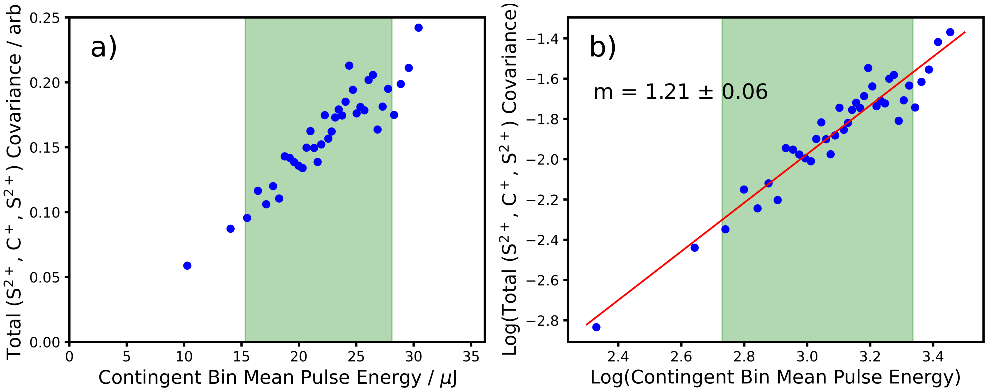

FIG. S19. Power dependence of the three-fold (S^{2+}, C^{+}, S^{2+}) covariance. a) Total covariance intensity as a function of the mean X-ray pulse energy within each contingent bin. b) Log-log plot of the logarithm of covariance intensity verses the logarithm of X-ray pulse energy. A linear fit (red line) to these data, alongside the extracted gradient, m, is shown. In both a) and b), the pulse energy region used in the main data analysis throughout the manuscript is highlighted in green.

To confirm that a distinct power dependence would be observed for channels which arise predominantly from the absorption of more than one X-ray photons, we repeated the analysis for the $S^{2+} + C^{+} + S^{2+}$ channel, which cannot be produced from a single S 2p core ionization and subsequent AM decays. As mentioned in the main manuscript, this channel is one of a number channels originating from higher charge states that are not analyzed in detail in the present study. This power-dependence analysis is presented in Figure S19. Here, a rather distinct power dependence is observed, with the covariance intensity signal clearly scaling with a higher polynomial of the X-ray pulse energy than for the dication and trication channels. This is confirmed by the extracted gradient from the log-log plot, which for this channel is 1.21 ± 0.06.

[1] J. P. Dahl and M. Springborg, The Morse oscillator in position space, momentum space, and phase space, The Journal of Chemical Physics **88**, 4535 (1988).

[2] L. Sun and W. L. Hase, Comparisons of classical and Wigner sampling of transition state energy levels for quasiclassical trajectory chemical dynamics simulations, The Journal of Chemical Physics **133** (2010).

[3] S. Mai, P. Marquetand, and L. González, Nonadiabatic dynamics: The SHARC approach, Wiley Interdisciplinary Reviews: Computational Molecular Science **8**, e1370 (2018).

[4] R. D. Johnson, Computational chemistry comparison and benchmark database, NIST standard reference database **101** (2022).

[5] T. Severt, J. Rajput, B. Berry, B. Jochim, P. Feizollah, B. Kaderiya, M. Zohrabi, F. Ziaee, K. R. P, D. Rolles, *et al.*, Native frames: An approach for separating sequential and concerted three-body fragmentation, Physical Review A **110**, 053104 (2024).

[6] J. Rajput, T. Severt, B. Berry, B. Jochim, P. Feizollah, B. Kaderiya, M. Zohrabi, U. Ablikim, F. Ziaee, K. Raju P, *et al.*, Native frames: Disentangling sequential from concerted three-body fragmentation, Physical Review Letters **120**, 103001 (2018).

[7] I. Gabalski, F. Allum, I. Seidu, M. Britton, G. Brenner, H. Bromberger, M. Brouard, P. H. Bucksbaum, M. Burt, J. P. Cryan, *et al.*, Time-resolved X-ray photoelectron spectroscopy: Ultrafast dynamics in CS_2 probed at the S 2p edge, The Journal of Physical Chemistry Letters **14**, 7126 (2023).

[8] J. Unwin, F. Allum, M. Britton, I. Gabalski, H. Bromberger, M. Brouard, P. H. Bucksbaum, T. Driver, N. Ekanayake, D. Garg, *et al.*, X-ray induced Coulomb explosion imaging of transient excited-state structural rearrangements in CS_2, Communications Physics **6**, 309 (2023).

[9] S. Ahmed and V. Kumar, Measurement of photoabsorption and fluorescence cross-sections for CS_2 at 188.2–213 and 287.5–339.5 nm, Pramana **39**, 367 (1992).

[10] R. Dalitz, CXII. On the analysis of τ-meson data and the nature of the τ-meson, The London, Edinburgh, and Dublin Philosophical Magazine and Journal of Science **44**, 1068 (1953).

[11] E. Wang, M. Gong, Z. Shen, X. Shan, X. Ren, A. Dorn, and X. Chen, Fragmentation dynamics of CS_2 in collisions with 1.0 keV electrons, The Journal of Chemical Physics **149** (2018).

[12] K. Saha, S. Banerjee, and B. Bapat, Three body dissociation of CS_2^{2+} subsequent to various S (2p) Auger transitions, The Journal of Chemical Physics **139** (2013).

[13] X. Wang, Y. Zhang, D. Lu, G. Lu, B. Wei, B. Zhang, Y. Tang, R. Hutton, and Y. Zou, Fragmentation of CO_2^{2+} in collisions with low-energy electrons, Physical Review A **90**, 062705 (2014).

[14] E. Wang, X. Shan, Z. Shen, M. Gong, Y. Tang, Y. Pan, K.-C. Lau, and X. Chen, Pathways for nonsequential and sequential fragmentation of CO_2^{3+} investigated by electron collision, Physical Review A **91**, 052711 (2015).

[15] N. Neumann, D. Hant, L. P. H. Schmidt, J. Titze, T. Jahnke, A. Czasch, M. Schöffler, K. Kreidi, O. Jagutzki, H. Schmidt-Böcking, *et al.*, Fragmentation Dynamics of CO_2^{3+} Investigated by Multiple Electron Capture in Collisions with Slow Highly Charged Ions, Physical review letters **104**, 103201 (2010).

[16] S. Srivastav, A. Sen, D. Sharma, and B. Bapat, Fragmentation dynamics of CO_2^{4+}: Contributions of different electronic states, Physical Review A **103**, 032821 (2021).

[17] K. Tiedtke, J. Feldhaus, U. Hahn, U. Jastrow, T. Nunez, T. Tschentscher, S. V. Bobashev, A. A. Sorokin, J. B. Hastings, S. Möller, L. Cibik, A. Gottwald, A. Hoehl, U. Kroth, M. Krumrey, H. Schöppe, G. Ulm, and M. Richter, Gas detectors for X-ray lasers, J. Appl. Phys. **103**, 094511 (2008).